

# Optical-to-Near-Infrared Simultaneous Observations for the Hot Uranus GJ3470b: A Hint for Cloud-free Atmosphere

Akihiko Fukui<sup>1</sup>, Norio Narita<sup>2</sup>, Kenji Kurosaki<sup>3</sup>, Masahiro Ikoma<sup>3</sup>, Kenshi Yanagisawa<sup>1</sup>, Daisuke Kuroda<sup>1</sup>, Yasuhiro Shimizu<sup>1</sup>, Yasuhiro H. Takahashi<sup>2,4</sup>, Hiroshi Ohnuki<sup>5</sup>, Masahiro Onitsuka<sup>6</sup>, Teruyuki Hirano<sup>7</sup>, Takuya Suenaga<sup>6</sup>, Kiyoe Kawauchi<sup>2</sup>, Shogo Nagayama<sup>2</sup>, Kouji Ohta<sup>8</sup>, Michitoshi Yoshida<sup>9</sup>, Nobuyuki Kawai<sup>10</sup>, Hideyuki Izumiura<sup>1</sup>

afukui@oao.nao.ac.jp

## ABSTRACT

We present optical ( $g'$ ,  $R_c$ , and  $I_c$ ) to near-infrared ( $J$ ) simultaneous photometric observations for a primary transit of GJ3470b, the second lowest-mass planet among transiting planets around nearby M dwarfs, by using the 50-cm MITSuME telescope and the 188-cm telescope both at Okayama Astrophysical Observatory. From these data, we derive the planetary mass, radius, and density as  $14.1 \pm 1.3 M_\oplus$ ,  $4.32^{+0.21}_{-0.10} R_\oplus$ , and  $0.94 \pm 0.12 \text{ g cm}^{-3}$ , respectively, thus confirming the low density that was reported by Demory et al. based on the *Spitzer*/IRAC 4.5- $\mu\text{m}$  photometry ( $0.72^{+0.13}_{-0.12} \text{ g cm}^{-3}$ ). Although the planetary radius is about 10% smaller than that reported by Demory et al., this difference does not alter their conclusion that the planet possesses a hydrogen-rich envelope whose mass is approximately 10% of the planetary total mass. On the other hand, we find that the planet-to-star radius ratio ( $R_p/R_s$ ) in the  $J$  band ( $0.07577^{+0.00072}_{-0.00075}$ ) is smaller than that in the  $I_c$  ( $0.0802 \pm 0.0013$ ) and 4.5- $\mu\text{m}$

---

<sup>1</sup>Okayama Astrophysical Observatory, National Astronomical Observatory of Japan, Asakuchi, Okayama 719-0232, Japan

<sup>2</sup>National Astronomical Observatory of Japan, 2-21-1 Osawa, Mitaka, Tokyo 181-8588

<sup>3</sup>Department of Earth and Planetary Science, The University of Tokyo, 7-3-1 Bunkyo-ku, Tokyo 113-0033, Japan

<sup>4</sup>Department of Astronomy, The University of Tokyo, 7-3-1 Hongo, Bunkyo-ku, Tokyo 113-0033

<sup>5</sup>Department of Earth and Planetary Sciences, Tokyo Institute of Technology, 2-12-1 Ookayama, Meguro-ku, Tokyo 152-8551

<sup>6</sup>The Graduate University for Advanced Studies, 2-21-1 Osawa, Mitaka, Tokyo 181-8588

<sup>7</sup>Department of Physics, The University of Tokyo, 7-3-1 Hongo, Bunkyo-ku, Tokyo 113-0033

<sup>8</sup>Dept. of Astronomy, Kyoto University, Kitashirakawa-Oiwake, Sakyo, Kyoto, 606-8502, Japan

<sup>9</sup>Hiroshima Astrophysical Science Center, Hiroshima University 1-3-1, Kagamiyama, Higashi-Hiroshima, Hiroshima, 739-8526, Japan

<sup>10</sup>Dept. of Physics, Tokyo Institute of Technology, 2-12-1, Ookayama, Meguro, Tokyo, 152-8551, Japan

( $0.07806^{+0.00052}_{-0.00054}$ ) bands by  $5.9 \pm 2.0\%$  and  $3.0 \pm 1.2\%$ , respectively. A plausible explanation for the differences is that the planetary atmospheric opacity varies with wavelength due to absorptions and/or scattering by atmospheric molecules. Although the significance of the observed  $R_p/R_s$  variations is still low, if confirmed, this fact would suggest that GJ3470b does not have a thick cloud layer in the atmosphere. This property would offer a wealth of opportunity for future transmission spectroscopic observations of this planet to search for certain molecular features without being prevented by clouds.

*Subject headings:* planetary systems — planets and satellites: atmosphere — planets and satellites: individual(GJ3470b) — stars: individual(GJ3470) — techniques: photometric

## 1. INTRODUCTION

Transiting extrasolar planets provide much valuable information, not only planetary mass and radius, but also planetary atmospheric composition. Because the optical thickness of a planetary atmosphere varies with wavelength depending on the atmospheric composition, one can probe atmospheric constituents by measuring transit radii with different wavelengths (e.g. Seager & Sasselov 2000; Brown 2001).

So far, this technique, known as the transmission spectroscopy, has been applied for several transiting hot Jupiters orbiting nearby bright host stars, as represented by HD 209458b and HD 189733b. In the atmosphere of HD 209458b, past observations detected many absorption and scattering features such as Na (Charbonneau et al. 2002; Snellen et al. 2008), H (Vidal-Madjar et al. 2003), O, C (Vidal-Madjar et al. 2004), TiO, VO (Désert et al. 2008), H<sub>2</sub> (Lecavelier Des Etangs et al. 2008b), H<sub>2</sub>O (Beaulieu et al. 2010), and CO (Snellen et al. 2010). On the contrary, HD 189733b has been revealed to have a featureless transmission spectrum over optical to possibly near infrared regions (Pont et al. 2008; Sing et al. 2009; Désert et al. 2011b; Gibson et al. 2012), while absorption features of Na and H were detected (Redfield et al. 2008; Lecavelier Des Etangs et al. 2010). This featureless spectrum has been interpreted as Rayleigh scattering due to high-altitude haze which dominates over molecular features (Lecavelier Des Etangs et al. 2008a).

Recently, it has become possible to expand this technique to low-mass planets, often referred to as exo-Neptunes ( $10 \lesssim M_p/M_\oplus \lesssim 30$ ) and super-Earths ( $M_p/M_\oplus \lesssim 10$ ), thanks to the discoveries of transiting low-mass planets around nearby low-mass stars (M dwarfs). Because M dwarfs have smaller radii compared to Sun-like stars, they show deeper transits for a same-sized transiting planet, enabling us to obtain high signal-to-noise-ratio transit signals, which are needed for transmission spectroscopy, even for small planets. The first two such examples are GJ436b (Butler et al. 2004; Gillon et al. 2007) and GJ1214b (Charbonneau et al. 2009), both of which are orbiting nearby M dwarfs. They can be thought to be the representatives of exo-Neptunes and super-Earths, respectively, in the sense of their masses ( $\sim 23$  and  $\sim 6.6 M_\oplus$ , respectively). As for GJ436b, no firm

molecular feature has been detected by transmission spectroscopy probably because of difficulties due to instrumental systematics (Gibson et al. 2011) and stellar activity (Knutson et al. 2011), while a methane-poor and CO-rich atmospheric model has been supported (Knutson et al. 2011) by combining the interpretation of the dayside spectrum obtained via secondary eclipse observations (Stevenson et al. 2010). The super-Earth GJ1214b has received much more attention since its discovery. Intensive observations by many observational groups have revealed that GJ1214b has a flat spectrum over optical to infrared wavelengths (e.g. Désert et al. 2011a; Bean et al. 2011; Berta et al. 2012; de Mooij et al. 2012; Narita et al. 2012; Fraine et al. 2013). This flat spectrum has been interpreted as the consequence of either a water-dominated atmosphere or a hydrogen-dominated but hazy/cloudy atmosphere, although which model is correct is still an open question (e.g. Howe & Burrows 2012).

GJ3470b, the target of this paper, is the third low-mass ( $< 30M_{\oplus}$ ) transiting planet discovered among nearby ( $< 35$  pc) M dwarfs (Bonfils et al. 2012) that provides a great opportunity of extending the atmospheric study for low-mass planets. Because its mass,  $\sim 14M_{\oplus}$ , is intermediate between those of GJ436b and GJ1214b, this planet should be a good sample for comparative study of atmospheric properties of low-mass planets. Demory et al. (2013) (hereafter D13) have recently reported follow-up observations for this system including *Spitzer*/IRAC 4.5- $\mu$ m photometry of two primary transits of GJ3470b. They precisely determined the planetary mass and radius as  $13.9^{+1.5}_{-1.4}M_{\oplus}$  and  $4.83^{+0.22}_{-0.21}R_{\oplus}$ , respectively, revealing its very low density ( $\rho_p = 0.72^{+0.13}_{-0.12}$  g cm $^{-3}$ ). This implies that GJ3470b has a light-gas atmosphere with enlarged spectrum features, thus making this planet as an attractive target for transmission spectroscopic studies. Nonetheless, no such study for this planet has been reported yet.

Here we present optical-to-near-infrared simultaneous photometric observations for a primary transit of GJ3470b obtained by using the 188-cm telescope and the 50-cm MITSuME telescope both at Okayama Astrophysical Observatory. The simultaneous observations have a great advantage for transmission-spectroscopic study. If the host star has cool star-spots on its surface, transit depth (square of planet-star radius ratio) can vary with time due to the variations of apparent luminous area of the star according to the stellar rotation and appearing/vanishing of the star-spots (e.g. Pont et al. 2008). This changes the apparent planetary radius with time. Therefore, the simultaneous observations enable us to investigate the wavelength dependence of planetary radius without concern for this star-spot effect.

The rest of this paper is organized as follows. We describe our observations in Section 2, followed by data reduction and analysis in Section 3 and Section 4, respectively. We discuss implications from our results in Section 5, and summarize this study in Section 6.

## 2. OBSERVATIONS

### 2.1. ISLE *J*-band Observations

We conducted *J*-band photometric observations for GJ3470 on the expected transit night of 2012 November 15, by using the near-infrared imaging and spectroscopic instrument ISLE (Yanagisawa et al. 2006, 2008), which is mounted on the Cassegrain focus of the 188 cm telescope at Okayama Astrophysical Observatory in Japan. ISLE has a  $1,024 \times 1,024$  HgCdTe HAWAII-1 array with the pixel scale of  $0''.245 \text{ pixel}^{-1}$ , providing the field of view of  $4'.3$  on a side. For relative photometry, we introduced a comparison star (2MASS:07591316+1525479,  $J=8.73$ ) onto the detector simultaneously with the target star GJ3470, where the two stars are separated by  $2'.9$ . At the beginning of the observations, the stellar positions on the detector were carefully set so that the both stellar images did not cover any bad pixels. During the observations, the telescope was defocused so that the full width at half maximum of the stellar point spread function (PSF) was  $\sim 20$  pixel, or  $\sim 5''$ , in order to mitigate the incompleteness of pixel-to-pixel-sensitivity (flat-fielding) correction and to extend the exposure time as long as possible while avoiding saturation. The exposure time was set to 30 sec, with which the peak analog-to-digital-unit (ADU) count of the brighter star (the comparison star) is well below the threshold of 25,000 ADU, above which the AD converting relation deviates more than 1% from a linear relation. The dead time including readout time for each exposure was 6 s. An observing log is shown in Table 1.

The 188-cm telescope is equipped with an offset guider system on the Cassegrain focus, which can correct the telescope tracking error every one second at minimum by using a fast-readout CCD camera which can keep track of a bright star coming into the surrounding area of the main detector. However, it had been recognized from past observations with ISLE that the stellar centroid positions on the ISLE detector slightly (a few pixels) changed over several hours even when the guiding system was activated<sup>1</sup>. This slight stellar displacement had introduced systematic errors into photometry. In order to correct this effect, we have developed an offset-correcting system which corrects the reference point of the guide star on the guiding camera, by calculating the displacement of stellar centroids on the last ISLE images relative to a reference image. Each correction needs an additional dead time for ISLE of 8 s. For the transit observations of GJ3470b, we activated this system with the frequency of the offset correction as once in 10 ISLE exposures. As a result, the stellar centroid change during the observations was well suppressed with 1.1 and 0.6 pixels in root mean square (RMS) for the X (right ascension) and Y (declination) directions, respectively. The centroid variation with time on the night is shown in Figure 1.

---

<sup>1</sup>We attributes the cause of this stellar displacement to a relative mechanical offset between the ISLE detector and the guiding CCD camera depending on the telescope position, rather than other effects such as the differential atmospheric refraction between infrared and optical wavelengths.

## 2.2. MITSuME Optical Observations

At the same time with the ISLE J-band observations, we also conducted photometric observations for the same transit of GJ3470b in optical wavelengths by using the 50-cm MITSuME telescope at Okayama Astrophysical Observatory. The telescope is equipped with three  $1024 \times 1024$  pixels CCD cameras, enabling to obtain  $I_c$ ,  $R_c$ , and  $g'$  band images simultaneously (Kotani et al. 2005; Yanagisawa et al. 2010). The each camera has the pixel scale of  $1''.5 \text{ pixel}^{-1}$  for the field of view of  $26' \times 26'$ .

The telescope was defocused so that the FWHM of stellar PSF is about 10 pixels, or  $\sim 15''$ , for the same purpose as the ISLE observations. We note that the contamination light from objects surrounding the target star is negligible because there is no object brighter than 20 and 16 magnitudes in any band within  $10''$  and  $20''$ , respectively, from GJ3470 in the SDSS photometric catalog (Adelman-McCarthy & et al. 2011). The exposure time was set to 60 s. The dead time including readout time for each exposure was 3 s for all bands. The observing log is compiled in Table 1.

Because this telescope has no mechanical auto-guiding system and previously caused large tracking error ( $\sim 100$  pixels) over several hours, we have developed a self-guiding software which calculates the displacement of stellar centroid positions on the last-observed  $I_c$ -band image relative to a reference image, then feeds back it to the telescope to correct the tracking error soon after the last image is obtained. By using this self-guiding software, the stellar centroid displacement during the observations for GJ3470 were kept with 1.4 and 0.5 pixels in RMS for X (right ascension) and Y (declination) directions, respectively, for all the three bands.

## 3. DATA REDUCTION

### 3.1. Reduction and Baseline Correction for the ISLE data

The obtained ISLE images are reduced by the standard procedure, including dark-image subtraction and flat-fielding correction. For the flat-fielding correction, 100 dome-flat images obtained on the observing night are used to create a flat-fielding image. Then, aperture photometry is done for the target and comparison star on the reduced images by using a customized tool (Fukui et al. 2011), applying a constant aperture radius for all images. A light curve is created by dividing GJ3470's fluxes by comparison's ones. We eliminate apparent outliers due to such as passing clouds and cosmic-ray hitting from the light curve. The time for each data point is assigned as the mid time of each exposure in the time system of Barycentric Julian Day (BJD) based on Barycentric Dynamical Time (TDB), which is converted from the time stamp recorded on the FITS header in the time system of Julian Day (JD) based on Coordinated Universal Time (UTC) by using the code of Eastman et al. (2010).

In order to select an appropriate aperture radius, we create a number of trial light curves with changing the aperture radius by 1 pixel, and evaluate the dispersion of the out-of-transit (OOT)

part of these trial light curves. We find that the light curve produced with the aperture radius of 34 pixels gives the minimum dispersion, and therefore use this light curve for further analyses. The selected light curve is shown in Figure 1. Subsequently, in order to correct the systematic trend in the light curve, which is apparent in the OOT light curve, we take the following procedure. First, we fit the OOT light curve with several baseline models given by the following formulae:

$$F_{\text{base}} = k_0 \times 10^{-0.4\Delta m_{\text{corr}}}, \quad (1)$$

$$\Delta m_{\text{corr}} = \sum_{i=1} k_i X_i, \quad (2)$$

where  $F_{\text{base}}$  is the baseline flux,  $\{\mathbf{X}\}$  are variables, and  $\{\mathbf{k}\}$  are coefficients. Generally, systematic trends could arise due to airmass change, slow variability of GJ3470 and/or the comparison star themselves, and stellar displacement on the detector. Therefore, for the variables  $\{\mathbf{X}\}$ , we test several combinations of  $z$ ,  $t$ ,  $t^2$ ,  $dx$ , and  $dy$ , where  $z$  is airmass,  $t$  is time,  $dx$  and  $dy$  are the relative centroid positions in  $x$  and  $y$  directions, respectively. Next, we evaluate the Bayesian information criteria (BIC; Schwarz 1978) for the respective baseline models. The BIC value for the OOT light curve is given by  $\text{BIC}_{\text{oot}} \equiv \chi_{\text{oot}}^2 + k \ln N_{\text{oot}}$ , where  $\chi_{\text{oot}}^2$  is the  $\chi^2$  value of the baseline fit for the OOT part,  $k$  is the number of free parameters, and  $N_{\text{oot}} = 155$  is the number of OOT data points. We find that the  $\{\mathbf{X}\} = \{z, dx, dy\}$  model gives the minimum  $\text{BIC}_{\text{oot}}$  value among all the baseline models, and therefore apply this model to correct the systematic trend in the entire light curve. In Table 2, we list the  $\text{BIC}_{\text{oot}}$  values and the RMS of the OOT light curve ( $\text{RMS}_{\text{oot}}$ ) for the four representative baseline models of  $\{X\} = \{z\}$ ,  $\{z, dx, dy\}$ ,  $\{z, t, dx, dy\}$ , and  $\{t, t^2, dx, dy\}$ . Noticeably, including  $dx$  and  $dy$  in  $\{\mathbf{X}\}$  provides a significant improvement on both the  $\text{BIC}_{\text{oot}}$  and  $\text{RMS}_{\text{oot}}$  values, from  $\text{BIC}_{\text{oot}} = 224.2$  and  $\text{RMS}_{\text{oot}} = 1.61 \times 10^{-3}$  for the  $\{z\}$  model to  $\text{BIC}_{\text{oot}} = 171.4$  and  $\text{RMS}_{\text{oot}} = 1.35 \times 10^{-3}$  for the  $\{z, dx, dy\}$  model. This fact indicates that the stellar displacements on the detector produces significant systematics on the photometry, and the displacements during our observations were enough suppressed such that the systematics can be corrected, owing to the development of the offset-correction system (Section 2.1). In Figure 1, we also plot the the best-fit OOT light curve with the baseline model of  $\{\mathbf{X}\} = \{z, dx, dy\}$ , along with the time variations of  $z$ ,  $dx$ , and  $dy$ . The corrected light curve is shown in Figure 2.

The selected baseline model of  $\{\mathbf{X}\} = \{z, dx, dy\}$  is, however, not so significantly favored compared to other baseline models of  $\{t, z, dx, dy\}$  and  $\{t, t^2, dx, dy\}$ , given the  $\text{BIC}_{\text{oot}}$  difference of only  $\sim 5$ . Therefore, the choice of baseline model could be a cause of a systematic error on the final result, i.e., transit parameters. In order to evaluate the impact of this systematic effect, we fit the entire light curves corrected by different baseline models with a transit model, and compare the resultant parameters. The transit parameters we use are the planet-star radius ratio,  $R_p/R_s$ , the mid transit time,  $T_c$ , the semi-major axis normalized by the stellar radius,  $a/R_s$ , the impact parameter,  $b \equiv a \cos i/R_s$ , where  $i$  is the orbital inclination, and the coefficients for stellar limb-darkening effect. We adopt the orbital eccentricity and orbital period as  $e = 0$  and  $P = 3.33671$  days, respectively, from D13. For a stellar limb-darkening model, we use the quadratic limb-darkening law,  $I(\mu) = 1 - u_1(1 - \mu) - u_2(1 - \mu)^2$ , where  $I$  is the intensity,  $\mu$  is the cosine of the

angle between the line of sight and the line from the stellar center to the position of the stellar surface, and  $u_1$  and  $u_2$  are the coefficients. Because  $u_1$  and  $u_2$  are heavily correlated and can not independently be constrained well, we let  $u_1$  free while fix  $u_2$  at a theoretical value during the fitting process; we adopt  $u_2 = 0.255$ , which is the mean of the two values for  $\{T_{\text{eff}}, \log g_s\} = \{3600, 4.5\}$  and  $\{3600, 5.0\}$ , where  $T_{\text{eff}}$  (K) is the stellar effective temperature and  $\log g_s$  (cgs) is the stellar surface gravity, in the table given by Claret et al. (2012) (The  $T_{\text{eff}}$  and  $\log g_s$  values for GJ3470 were derived by D13 as  $3600 \pm 100$  and  $4.658 \pm 0.030$ , respectively). For calculating a transit model, we use the analytic formula given by Ohta et al. (2009), which is equivalent with that of Mandel & Agol (2002) when using the quadratic limb-darkening law. The best-fit parameters are determined by the AMOEBA algorithm (Press et al. 1992). In Figure 2, the best-fit transit model for the light curve corrected with the  $\{\mathbf{X}\} = \{z, dx, dy\}$  model is plotted. The photometric errors are rescaled so that the reduced  $\chi^2$  value for the best-fit transit model becomes unity.

The derived best-fit values and uncertainties of  $R_p/R_s$ ,  $a/R_s$ , and  $T_c$ , as well as the  $\chi^2$  values are listed in Table 2. While the  $\chi^2$  value for the  $\{\mathbf{X}\} = \{z\}$  model is relatively large as expected, those for the other three models of  $\{z, dx, dy\}$ ,  $\{z, t, dx, dy\}$ , and  $\{t, t^2, dx, dy\}$  are very close to each other. However, the  $R_p/R_s$  values for these three models are slightly different, with the largest difference of 0.00081 between  $\{z, dx, dy\}$  and  $\{t, t^2, dx, dy\}$ , which is comparable to the  $1\text{-}\sigma$  uncertainties of  $R_p/R_s$ . Therefore, we consider this discrepancy as a systematic error in  $R_p/R_s$ , and will be taken into account in the study of wavelength dependency of  $R_p/R_s$  discussed in Section 5.2. On the other hand, the baseline-model dependences on  $a/R_s$ ,  $b$ , and  $T_c$  are negligible compared to their  $1\text{-}\sigma$  uncertainties.

### 3.2. Reduction and Baseline Correction for the MITSuME data

The obtained MITSuME images are reduced in the same way as the ISLE images. For the flat-fielding correction, 27 twilight-flat images for each band obtained on the observing night are used to create each flat-fielding image. We then apply aperture photometry for GJ3470 and dozens of bright stars on the reduced images, with a number of trial aperture radii incremented by 0.5 pixels. Among a number of combinations of aperture radii and comparison stars, we first visually select several good combinations which produce less-dispersed light curves with respect to a transit signature. Next, we fit each trial light curve including the transit part with a transit + a tentative-baseline model, and select the least-dispersed light curve as the most appropriate one for each band. The reason of including the transit part is that, unlike the  $J$ -band data, the MITSuME data do not have enough number of OOT data. For the tentative baseline model, we use Equation (1) and (2) with  $\{\mathbf{X}\} = \{z\}$ . As for the transit model, we use the same parameterization as Section 3.1. For the  $I_c$ - and  $R_c$ -band data, we fix  $u_2$  at the theoretical values of 0.338 and 0.322, respectively, while let  $u_1$  free during the fitting process. For the  $g'$ -band data, we fix both  $u_1$  and  $u_2$  at the theoretical values of 0.486 and 0.289, respectively, because it is too poor to constrain  $u_1$  nor  $u_2$  by the current data. These theoretical values are derived by the same way as for the  $J$ -band data. In

addition, we force  $a/R_s$  and  $b$  to the values derived from D13, namely 13.4 and 0.40, respectively. This is because the *Spitzer*’s data used by D13 is more precise than the MITSuME’s data, and we are more focusing on studying the wavelength dependence of  $R_p/R_s$  (see Section 5.2) rather than constraining other parameters. As a result, we select the light curves produced with the aperture radii of 7.0, 8.0, and 6.0 pixels, and the number of comparison stars of 4, 10, and 8, for  $I_c$ ,  $R_c$ , and  $g'$  bands, respectively. We note that these results are robust over different baseline models.

Subsequently, in order to select appropriate baseline models for correcting systematic trends, we again fit the selected light curves with a transit + several baseline models. At this time, we test the three baseline models of  $\{\mathbf{X}\} = \{z\}$ ,  $\{z, t\}$ , and  $\{t, t^2\}$ . We do not include  $dx$  and  $dy$  in  $\{\mathbf{X}\}$  because we do not find any improvement for any bands when we preliminary fit the light curves by including  $dx$  and  $dy$ . In Table 3, we list the resultant BIC and RMS values for the three baseline models for each band. For the  $I_c$  and  $g'$  bands, we find that the baseline model of  $\{\mathbf{X}\} = \{z\}$  gives the minimum BIC values, and therefore adopt it for correcting the systematic trends in these light curves. On the other hand, for the  $R_c$ -band data, all the three baseline models give almost the same BIC values, indicating that the three models have the same statistical significance. So, we decide to select the model  $\{\mathbf{X}\} = \{z, t\}$  among the three models, based on the fact that the RMS values for  $\{z, t\}$  and  $\{t, t^2\}$  ( $2.46 \times 10^{-3}$ ) are slightly better than that for  $\{z\}$  ( $2.50 \times 10^{-3}$ ), and it is physically more straightforward to include airmass in the variables rather than just a polynomial function of time.

As also discussed in Section 3.1, the selection of baseline models could affect on the final result. In Table 3, we also list the resultant  $R_p/R_s$  values for the respective models for each band. The largest differences of  $R_p/R_s$  are 0.0014, 0.0060, and 0.009, for the  $I_c$ ,  $R_c$ , and  $g'$  bands, respectively. The differences for the  $I_c$  and  $g'$  bands are comparable to and less than the  $1\text{-}\sigma$  uncertainties of  $R_p/R_s$ , respectively, while that for the  $R_c$  band is more than 3 times the  $1\text{-}\sigma$  uncertainty of  $R_p/R_s$ . These possible systematic offsets will be considered in the discussion on the wavelength dependence of  $R_p/R_s$  in Section 5.2.

In Figure 3, we show the uncorrected light curves and the best-fit transit+baseline models of the three bands, as well as their residuals. After the baseline for each light curve is corrected, error bars are rescaled so that the reduced  $\chi^2$  for a transit-model fit becomes unity.

## 4. ANALYSIS

In order to derive the final transit parameters and their uncertainties, we analyze the corrected  $J$ -,  $I_c$ -,  $R_c$ -, and  $g'$ -band light curves simultaneously by the Markov Chain Monte Carlo (MCMC) method by using a customized code (Narita et al. 2012). In this analysis, we treat  $b$ ,  $a/R_s$ , and  $T_c$  as common parameters for all the four light curves, while  $R_p/R_s$ ,  $u_1$ ,  $u_2$  as independent parameters for the respective light curves so as to take the wavelength dependences of these parameters into account. The values of  $b$ ,  $a/R_s$ ,  $T_c$ , and each  $R_p/R_s$  for each band are left free during the MCMC



process. The  $u_1$  and  $u_2$  values are treated the same way as previously;  $u_1$  for the  $J$ ,  $I_c$ , and  $R_c$  bands is left free, while  $u_1$  for the  $g'$  band and  $u_2$  for all the bands are fixed at the theoretical values. We adopt  $e = 0$  and  $P = 3.33671$  days in the same way as previously.

In a MCMC chain, we start with a set of parameters which provides the minimum  $\chi^2$  value determined by the AMOEBA algorithm. The  $\chi^2$  value is given by

$$\chi^2 = \sum_i \left( \frac{f_{\text{obs},i} - f_{\text{model}}}{\sigma_i} \right)^2, \quad (3)$$

where  $f_{\text{obs},i}$  is the  $i$ -th photometric flux,  $\sigma_i$  is the  $i$ -th photometric error, and  $f_{\text{model}}$  is the model flux calculated from the given parameter set. Then, the next parameter set is randomly selected, where we assume gaussian distributions whose means are the respective current values and standard deviations are proportional to their  $1\text{-}\sigma$  errors. This parameter set is always accepted when it gives  $\Delta\chi^2 < 0$ , where  $\Delta\chi^2$  is the  $\chi^2$  difference between the next parameter set and current one; otherwise it is accepted according to an acceptance probability which is given by  $p = \exp^{\Delta\chi^2/2}$ . This process (link) is repeated for  $10^6$  times in a chain, from which the first  $10^5$  links are removed as a burn-in portion. The widths of the gaussian distributions for jumping parameters are set so that the acceptance ratio becomes about 25%. We run 10 independent chains, and create merged posterior distributions of the respective parameters. We define  $1\text{-}\sigma$  statistical uncertainties as the range of parameters between 15.87% and 84.13% of the posterior distributions. The resultant values and uncertainties are listed in Table 4, and two-dimensional 68.3% and 99.7% confidence regions for selected parameters drawn from the posterior distributions are shown as red contours in Figure 4. The derived model light curves for the respective bands are shown in Figure 5, along with the observed data binned in 5-minute intervals.

We confirm that the values of  $b$ ,  $a/R_s$ , and  $R_p/R_s$  for  $I_c$ ,  $R_c$ , and  $g'$  bands are all consistent with those reported by D13 within  $2\sigma$ . On the other hand, we find that the  $R_p/R_s$  value for the  $J$ -band data,  $0.07536 \pm 0.00079$ , is inconsistent with that for the  $I_c$ -band data of  $0.0797 \pm 0.0014$  by  $2.6\sigma$ , and also inconsistent with that for the *Spitzer*'s  $4.5\text{-}\mu\text{m}$  data of  $0.07806^{+0.00052}_{-0.00054}$  by  $2.8\sigma$ . One possibility of these discrepancies is a systematic effect originated from stellar activity (e.g. Czesla et al. 2009). Occulting cool star-spots by a transiting planet can induce a bump in the transit light curve, easily affecting the fitted parameters. Although we cannot identify any such feature in any of our light curves nor the *Spitzer*'s ones, if the planet occulted cool spots existing near the stellar limb, they would be difficult to be identified, and cause systematic offsets on the derived transit parameters such as  $b$ , which is weakly correlated with  $R_p/R_s$  (see Figure 4). This might be the case, because the  $b$  value derived from our data ( $< 0.281$  as  $1\text{-}\sigma$  upper limit) is slightly inconsistent with that by D13 ( $0.40^{+0.06}_{-0.08}$ ) by more than  $1\sigma$ . In order to reduce such a systematical effect on  $R_p/R_s$ , we repeat the MCMC analysis by using the  $b$  value reported by D13 as a prior information. In this analysis, we use the following function instead of Equation (3) for calculating

the  $\chi^2$  value:

$$\chi^2 = \sum_i \left\{ \left( \frac{f_{\text{obs},i} - f_{\text{model}}}{\sigma_i} \right)^2 + \left( \frac{b - b_{\text{prior}}}{\sigma_{b_{\text{prior}}}} \right)^2 \right\}, \quad (4)$$

where we adopt  $b_{\text{prior}} = 0.40$ , and  $\sigma_{b_{\text{prior}}} = 0.06$  if  $(b - b_{\text{prior}}) > 0$ ; otherwise  $\sigma_{b_{\text{prior}}} = 0.08$ . The resultant values and uncertainties are summarized in Table 4, and the two-dimensional correlation maps for selected parameters are plotted as blue contours in Figure 4. As a result, we find that our  $b$  and  $a/R_s$  values become consistent with those by D13 within  $1\sigma$ . However, although the  $R_p/R_s$  values for our data ( $J$ ,  $I_c$ ,  $R_c$ , and  $g'$  bands) become to be closer to that for the  $4.5\text{-}\mu\text{m}$  band, there are still disagreement between  $J$  and  $I_c$  by  $2.5\sigma$ , and between  $J$  and  $4.5\text{ }\mu\text{m}$  by  $2.6\sigma$ . In principle, these discrepancy could be due to the wavelength dependence of the planetary atmospheric opacity. This will be discussed in Section 5.2.

## 5. DISCUSSIONS

### 5.1. Physical Parameters of the Planetary System

In this section, we focus on the physical parameters of the planetary system. One of our goals in this section is to test the very low density of GJ3470b suggested by D13 with our independent observations, and therefore we here discuss along the results of the MCMC analysis without  $b$  prior.

First, we refine the orbital period by a linearly fit to our  $T_c$  value and the D13's one (they reported one reference transit mid-time). The resultant orbital period is  $P = 3.336651 \pm 0.000005$  days, which is consistent with  $P = 3.33671 \pm 0.00005$  days derived by D13 based on the two transits observed by *Spitzer* and four transits from (Bonfils et al. 2012), with the difference of only  $5.1 \pm 4.3$  sec. This means that no transit timing variation exceeding  $4.0 \pm 3.4$  min is observed between the two epochs, which are separated by 47 transit epochs.

Next, we investigate the stellar mass and radius. The stellar density,  $\rho_s$ , can directly be derived from  $a/R_s$  and  $P$  via the following relation assuming a circular orbit:  $\rho_s = 0.01342 \times (a/R_s)^3 / (P(\text{days}))^2 \rho_\odot$ . From our MCMC results, we derive the stellar density as  $\rho_s = 3.83^{+0.14}_{-0.32} \rho_\odot$ , which is broadly consistent with the value derived by D13 ( $2.91^{+0.37}_{-0.33} \rho_\odot$ ) within  $2\sigma$ , although our value is 32% larger than that by D13. The stellar mass and radius can be derived from the stellar density, combined with one or more additional information such as a stellar color (or temperature), luminosity (i.e., apparent brightness and distance to the star), and/or a stellar mass-radius relation. Because a trigonometric parallax for GJ3470 has not been measured so far, D13 solved the stellar mass, radius, and parallax simultaneously from  $\rho_s$  and  $VJHK_s$  magnitudes, via two empirical relations of mass-luminosity (Delfosse et al. 2000) and diameter-color-luminosity (Kervella et al. 2004) relations. As a result, they derived the stellar mass and radius as  $M_s = 0.539^{+0.047}_{-0.043} M_\odot$  and  $R_s = 0.568^{+0.037}_{-0.031} R_\odot$ , respectively. However, the latter relation they adopted was derived from dwarf samples which contained relatively small number ( $< 15$ ) of low-mass (K-M) dwarfs. In addition,

metallicity dependence of this relation was not found in the samples (Kervella et al. 2004), however, Boyajian et al. (2012) have recently found, based on interferometric radius measurements for 33 single K-M dwarfs, that a color-radius relation for low-mass stars clearly depends on metallicity. Therefore, the relation adopted by D13 could potentially have a systematic offset. In Figure 6, we plot a mass-radius relation for low-mass stars provided by Boyajian et al. (2012) (green shaded region), which was derived based on the radius measurements for the 33 K-M dwarfs and an empirical mass-luminosity relation of Henry & McCarthy (1993), which is consistent with that of Delfosse et al. (2000). we also plot a mass-radius relation for GJ3470 drawn by connecting the two empirical relations that D13 adopted (light-blue shaded region), where  $K_s = 7.989$  is used for the mass-luminosity calibration and  $H = 8.206$  and  $(V - H) = 4.124$  are used for the diameter-color-luminosity calibration. These two relations do not cross each other, implying that some systematic offset could exist, possibly in the diameter-color-luminosity relation of Kervella et al. (2004) due to the small number of low-mass star samples and the unconsidered metallicity dependence.

Therefore, instead of using the same way as D13, we solve  $M_s$  and  $R_s$  from  $\rho_s$  by using the mass-radius relation of Boyajian et al. (2012) (Equation (4) in the paper). We note that any metallicity dependence of this relation was detected (Boyajian et al. 2012). In order to properly estimate  $M_s$ ,  $R_s$  and their uncertainties, we create probability distributions of these parameters by using a Monte Carlo (MC) technique. That is, the probability distributions are created by repeating the process that the values of  $a/R_s$  and three coefficients of the mass-radius relation are taken according to their respective probability distributions, and then  $M_s$  and  $R_s$  are solved. For the probability distribution of  $a/R_s$ , the posterior distribution created from the MCMC analysis is used, while for those of the three coefficients, gaussian distributions whose standard deviations are set to their 1- $\sigma$  errors are used. The resultant median values and the 68.3% confidence intervals are calculated as  $M_s = 0.557^{+0.028}_{-0.020} M_\odot$  and  $R_s = 0.526^{+0.023}_{-0.011} R_\odot$ . In Figure 6, we also plot the derived  $M_s$  and  $R_s$  values (red circle) as well as those reported by D13 (brown triangle). Our  $M_s$  and  $R_s$  values are both consistent with those by D13 within 1  $\sigma$ . However, this agreement is by coincidence, because the derived stellar density is slightly inconsistent between this work and D13 by more than 1  $\sigma$ , and the adopted calibration methods for deriving stellar mass and radius are different and also inconsistent between the two. Thus, further follow-up observations to confirm the stellar mass and radius would be valuable; photometric transit observations could test the stellar density, and astrometric observations for measuring the trigonometric parallax would provide a new insight into the stellar mass/radius calibration.

Finally, using the estimated  $M_s$  and  $R_s$ , we derive the relevant stellar and planetary parameters. For the planetary radius, we adopt the  $R_p/R_s$  value for  $J$  band. This is because not only the  $J$ -band light curve has the highest photometric precision among the four light curves, but also, as will be discussed in Section 5.2, the planetary radii for the optical bands could be enlarged due to putative atmospheric haze, and the smaller  $J$ -band planetary radius could represent a haze-free planetary radius. For the planetary mass, we use the following relation assuming a circular orbit:  $K' = (2\pi G)^{1/3} M_p \sin i / (M_s + M_p)^{2/3}$ , where  $K'$  is a parameter derived from radial-velocity data

and  $K' = 13.4 \pm 1.2 \text{ m s}^{-1} \text{ d}^{1/3}$  is adopted from D13. The  $M_p$  and  $R_p$  values as well as other stellar and planetary parameters (the stellar surface gravity,  $\log g_s$ , the semi-major axis,  $a$ , the planetary density,  $\rho_p$ , and the planetary surface gravity,  $g_p$ ) are derived by the same MC fashion as previously. The derived values and uncertainties are listed in Table 5. The planetary mass, radius, and density are derived as  $M_p = 14.1 \pm 1.3 M_\oplus$ ,  $R_p = 4.32^{+0.21}_{-0.10} R_\oplus$ , and  $\rho_p = 0.94 \pm 0.12 \text{ g cm}^{-3}$ , respectively. Although the planetary density is  $\sim 30\%$  larger than that by D13 ( $0.72^{+0.13}_{-0.12} \text{ g cm}^{-3}$ ), it is still well lower than that of Uranus ( $1.27 \text{ g cm}^{-3}$ ) despite of its similar mass ( $14.54 M_\oplus$ ), confirming the low density of GJ3470b, firstly suggested by Bonfils et al. (2012) and recently uncovered by D13. We note that the  $\sim 30\%$  difference of the planetary density comes mainly from the  $\sim 10\%$  smaller planetary radius (the  $\sim 7\%$  smaller stellar radius and the  $\sim 3\%$  smaller planet-star radius ratio) compared to D13. In Table 5, we also list the results derived from the MCMC analysis with  $b$  prior, for reference.

In order to investigate the impact of the 10% difference of the planetary radius on the planetary bulk composition, we have modeled the internal structure of GJ3470b that is consistent with the planetary mass and radius derived in this study. To do so, we have assumed that the planet is composed of three layers, namely, a cloud/haze-free hydrogen-rich atmosphere with solar composition, on top of an ice/water mantle, on top of a rocky core (the water/rock mass ratio is set to 3). Two-layered structure (hydrogen-rich atmosphere + rocky core) is also examined. The equations of state adopted are SCvH EOS for hydrogen/helium (Saumon et al. 1995), R-EOS (French et al. 2009) and SESAME EOS (Lyon & Johnson 1992) for water, and Valencia et al. (2007) for rock (details are described in Kurosaki et al. in prep). We have found that the mass fraction of the hydrogen-rich atmosphere ranges 5% to 9% in the three-layer models and 12% to 19% in the two-layer models. These values are similar with those derived in D13. Therefore, the 10% difference in radius does not alter their conclusion that the planet possesses a hydrogen-rich envelope the mass of which accounts for approximately 10% of the planetary total mass. We note that this conclusion may be consistent with recent theoretical prediction: If the atmosphere embedded in a protoplanetary disk grows in mass beyond 10% of the planetary total mass, its accretion tends to proceed in a runaway fashion (Ikoma & Hori 2012). Thus, nebular-origin atmospheres of  $>10\%$  of planetary mass are rarely detected.

## 5.2. Wavelength Dependence of the Planet-star Radius Ratio

In this section, we discuss the wavelength dependence of  $R_p/R_s$  based on the results of the MCMC analysis with  $b$  prior. In Figure 8, we plot the  $R_p/R_s$  values in the  $g'$ ,  $R_c$ ,  $I_c$ , and  $J$  bands, and that in the *Spitzer*'s  $4.5\text{-}\mu\text{m}$  band reported by D13, along with the transmission curves for the respective passbands. The  $R_p/R_s$  values in the  $I_c$  and  $4.5\text{-}\mu\text{m}$  bands are larger than that in the  $J$  band by  $5.9 \pm 2.0\%$  and  $3.0 \pm 1.2\%$ , respectively. Those in the  $g'$  and  $R_c$  bands are also larger than that in the  $J$  band, although the uncertainties in these bands are relatively large.

As discussed in Section 3.1 and 3.2, the choice of the baseline model could cause a systematic

offset in  $R_p/R_s$ . However, the alternative choices of the baseline models for the  $R_c$ -,  $I_c$ -, and  $J$ -band light curves work as expanding the discrepancies, as indicated by gray circles in Figure 8, meaning that the systematics due to the baseline selections cannot explain the observed discrepancies of  $R_p/R_s$ .

Unocculted star-spots can also vary apparent  $R_p/R_s$  with time, due to the variations of apparent luminous area of the star according to the stellar rotation and appearing/vanishing of the star-spots (e.g. Pont et al. 2008). Since the observational epochs are different with  $\sim 5$  months apart, there is a possibility that the observed  $R_p/R_s$  difference between the  $J$  and  $4.5\text{-}\mu\text{m}$  bands is caused by the star-spot effect. When a spotted host star induces the peak-to-valley variability of  $r \equiv R_p/R_s$ ,  $\Delta r$ , due to the unocculted star-spot effect, the host star itself will show a peak-to-valley flux variability of  $(1 + (\Delta r/r))^2 - 1$  with a period consistent with the stellar rotation period. Therefore, if the  $3.0 \pm 1.2\%$  difference of  $R_p/R_s$  between the  $J$  and  $4.5\text{-}\mu\text{m}$  bands were caused by star-spots, the host star would have to show at least  $6.0 \pm 2.3\%$  peak-to-valley intrinsic variability. In order to estimate the maximum intrinsic variability of the host star, we have conducted a long-term photometric monitoring for GJ3470 by using the 50-cm MITSuME telescope, spanning  $\sim 60$  days. The resultant  $I_c$ -band light curve is shown in Figure 7, along with the sky-flux variations. We have found that the RMS of the nightly-averaged fluxes is 0.33% and the peak-to-valley variability is merely  $\sim 1\%$ , indicating that GJ3470 is not a very active star and star-spot variations cannot account for the observed  $R_p/R_s$  difference between the  $J$  and  $4.5\text{-}\mu\text{m}$  bands, unless the stellar variability is unusually large only in infrared wavelength. In addition, the difference of  $R_p/R_s$  between the  $I_c$  and  $J$  bands cannot intrinsically be explained by the spot-rotation effect, because these data were obtained simultaneously. We note that a possible  $\sim 25$ -day periodic variation seen in the long-monitoring light curve could potentially be due to a star-spot rotation according to the stellar rotation, however, we have found that a part of the flux variations ( $\text{JD} \gtrsim 2,456,258$ ) could be correlated with the sky-flux variations, and therefore further monitoring is needed to confirm it (more will be investigated in a future paper).

More likely scenario would be that the planetary atmospheric opacity varies with wavelength due to absorptions and/or scattering by atmospheric molecules. The relative change in transit depth due to molecular absorptions as a function of wavelength can be approximated by  $\Delta D(\lambda) \sim 2n_H(\lambda)HR_p/R_s^2$ , where  $n_H(\lambda)$  is the scale factor depending on the molecular opacity, which can be  $\sim 10$  for strong absorbers (Brown 2001), and  $H$  is the atmospheric scale height given by  $H \equiv kT/\mu g_p$ , where  $k$  is Boltzmann’s constant,  $T$  is the atmospheric temperature, and  $\mu$  is the mean molecular weight. For GJ3470b,  $H \sim 250\text{--}400$  km when assuming  $T = 500\text{--}650\text{K}$  and a solar-composition atmosphere ( $\mu = 2.36$  atomic mass). Therefore,  $\Delta D(\lambda)$  can be up to  $\sim 0.16\%$ , which corresponds to the relative change in  $R_p/R_s$  of  $\sim 13\%$ , indicating that the observed differences of  $R_p/R_s$  can reasonably be explained by molecular absorptions. Indeed, there are strong absorption bands of CO and CO<sub>2</sub> around  $4.5\text{-}\mu\text{m}$ , which makes  $R_p/R_s$  in the  $4.5\text{-}\mu\text{m}$  band be larger. Therefore, the observational result that  $R_p/R_s$  in the  $4.5\text{-}\mu\text{m}$  band is larger than that in the  $J$  band is qualitatively consistent with a CO- and/or CO<sub>2</sub>-containing atmosphere. On one hand, the

larger  $R_p/R_s$  values in the optical ( $I_c$ ,  $R_c$ , and  $g'$ ) bands compared to that in the  $J$  band could be explained by Rayleigh scattering due to molecular hydrogen or small-sized ( $\lesssim 0.1 \mu\text{m}$ ) haze in the atmosphere, as is the case for HD 209458b (Lecavelier Des Etangs et al. 2008b) and HD 189733b (Pont et al. 2008). Especially, the transition wavelength below which the spectrum begins to rise due to Rayleigh scattering is around  $1 \mu\text{m}$  for  $\sim 0.1\text{-}\mu\text{m}$  sized haze particles (e.g. Howe & Burrows 2012), and therefore the observed  $R_p/R_s$  difference between the  $I_c$  and  $J$  bands could be explained well by such a hazy atmospheric model. In Figure 8, we also plot a model spectrum which qualitatively fits the data (blue dotted line). For the model spectrum, we adopt a model provided by Howe & Burrows (2012) in which a  $0.3 \times$  solar-abundance atmosphere with  $T = 700\text{K}$  containing  $0.1\text{-}\mu\text{m}$  tholin particles with a density of  $1000 \text{ cm}^{-3}$  is assumed, and scale it so as to fit the scale height of GJ3470b. We note that a quantitative discussion and fine-tuning of this model is beyond the scope of this paper, and to do so, further observational data are required.

The observed  $R_p/R_s$  variations also indicate that the planet would have no thick clouds in the sky, because if the atmosphere of GJ3470b were covered by thick clouds at high altitudes, a much flat spectrum over optical to infrared wavelengths would be observed (e.g. Berta et al. 2012). If true, this fact would offer a wealth of opportunity to probe many molecular features in the GJ3470b’s atmosphere through high-precision transmission spectroscopic observations, without being prevented by thick clouds. On the other hand, a constant fit to the observed five  $R_p/R_s$  values yields the  $\chi^2$  value of 11.6, meaning that the statistical probability of exceeding this  $\chi^2$  value assuming gaussian errors is 2.1%. Thus, a fully-clouded atmospheric model still cannot be ruled out by the current data.

We should note that this is the first report on transit observations by using the 188-cm telescope/ISLE instrument and the 50-cm MITSuME telescope. Our observations for GJ3470b demonstrate that these telescopes/instruments are quite useful for studying transiting planets, especially for probing planetary atmospheres by simultaneous observations through the optical to near-infrared wavelengths. Nevertheless, the capability of the 50-cm MITSuME telescope is limited due to the limited aperture size. It would be a great capability if 2-4 m class telescopes like the 188-cm telescope are equipped with a transit-dedicated camera which can take multi-color images through optical to infrared simultaneously. The GROND instrument, mounted on the MPG/ESO 2.2-m telescope in Chile (Greiner et al. 2008), is a pioneer for such an ambitious instrument, which can obtain seven images through  $g'$  to  $K$  bands simultaneously for the southern hemisphere. Recently, simultaneous transit observations by using the GROND instrument have been reported (Mancini et al. 2013; de Mooij et al. 2012), demonstrating the usefulness of such a multi-color imager for transit observations. However, this instrument had originally been developed for catching gamma-ray-burst afterglows and not been designed for high-precision transit observations (Mancini et al. 2013). Future developments of such instruments, but more dedicated to transit observations, for 2-4 m class telescopes in northern hemisphere will provide fruitful results on the exoplanetary atmospheric studies.

## 6. SUMMARY

We have presented optical ( $g'$ ,  $R_c$ , and  $I_c$ ) to near-infrared ( $J$ ) simultaneous photometric observations for a primary transit of the hot Neptune GJ3470b, by using the 188-cm telescope/ISLE instrument and the 50-cm MITSuME telescope both at Okayama Astrophysical Observatory. We have found that the planetary density is broadly consistent with that reported by Demory et al. (2013) (D13), who measured it based on the *Spitzer*/IRAC 4.5- $\mu$ m photometry, confirming its low density. Although the derived planetary radius is about 10% smaller than that reported by D13, this difference does not alter their conclusion that the planet possesses a hydrogen-rich envelope whose mass is approximately 10% of the planetary total mass. On the other hand, we have found that the planet-to-star radius ratio ( $R_p/R_s$ ) in the  $J$  band is smaller than that in the  $I_c$  and 4.5- $\mu$ m bands by  $5.9 \pm 2.0\%$  and  $3.0 \pm 1.2\%$ , respectively. These discrepancies cannot be explained by systematic effects due to baseline corrections. In addition, we have found from a long-term flux monitoring for GJ3470b that the intrinsic peak-to-valley stellar variability in  $I_c$  band is mealy  $\sim 1\%$ , indicating that the unocculted star-spot effect is unlikely to account for the observed  $R_p/R_s$  difference between the  $J$  and 4.5- $\mu$  bands. Instead, Rayleigh scattering due to molecular hydrogen or small-sized ( $\lesssim 0.1 \mu\text{m}$ ) haze in the atmosphere and molecular absorptions such as CO and CO<sub>2</sub> could reasonably explain the observed  $R_p/R_s$  variations. Although the significance is still low, if these  $R_p/R_s$  variations are confirmed, this fact would suggest that GJ3470b would not have a thick cloud layer in the atmosphere, offering a wealth of opportunity for future transmission-spectroscopic observations to probe many molecular features in the atmosphere of the hot Neptune.

We note that this is the first report on transit observations by using the 188-cm telescope/ISLE instrument and the 50-cm MITSuME telescope. Our observations demonstrate that optical-to-near-infrared simultaneous observations using such as these instruments are very useful for planetary atmospheric studies. Future developments of multicolor imagers for 2-4 m class telescopes in northern hemisphere would provide much more fruitful results for this field.

We thank Y. Hori for valuable discussions. We acknowledge a support by NINS Program for Cross-Disciplinary Study. N.N. is supported by NAOJ Fellowship and by the JSPS Grant-in-Aid for Research Activity Start-up No. 23840046. Y.H.T and T.H are supported by JSPS Fellowships for Research (DC1: 23-271 and 22-5935, respectively).

## REFERENCES

- Adelman-McCarthy, J. K., & et al. 2011, VizieR Online Data Catalog, 2306, 0
- Bean, J. L., et al. 2011, ApJ, 743, 92
- Beaulieu, J. P., et al. 2010, MNRAS, 409, 963
- Berta, Z. K., et al. 2012, ApJ, 747, 35

- Bonfils, X., et al. 2012, *A&A*, 546, A27
- Boyajian, T. S., et al. 2012, *ApJ*, 757, 112
- Brown, T. M. 2001, *ApJ*, 553, 1006
- Butler, R. P., Vogt, S. S., Marcy, G. W., Fischer, D. A., Wright, J. T., Henry, G. W., Laughlin, G., & Lissauer, J. J. 2004, *ApJ*, 617, 580
- Charbonneau, D., Brown, T. M., Noyes, R. W., & Gilliland, R. L. 2002, *ApJ*, 568, 377
- Charbonneau, D., et al. 2009, *Nature*, 462, 891
- Claret, A., Hauschildt, P. H., & Witte, S. 2012, *A&A*, 546, A14
- Czesla, S., Huber, K. F., Wolter, U., Schröter, S., & Schmitt, J. H. M. M. 2009, *A&A*, 505, 1277
- de Mooij, E. J. W., et al. 2012, *A&A*, 538, A46
- Delfosse, X., Forveille, T., Ségransan, D., Beuzit, J.-L., Udry, S., Perrier, C., & Mayor, M. 2000, *A&A*, 364, 217
- Demory, B.-O., et al. 2013, *ArXiv e-prints*
- Désert, J.-M., Vidal-Madjar, A., Lecavelier Des Etangs, A., Sing, D., Ehrenreich, D., Hébrard, G., & Ferlet, R. 2008, *A&A*, 492, 585
- Désert, J.-M., et al. 2011a, *ApJ*, 731, L40
- . 2011b, *A&A*, 526, A12
- Eastman, J., Siverd, R., & Gaudi, B. S. 2010, *PASP*, 122, 935
- Fraine, J. D., et al. 2013, *ArXiv e-prints*
- French, M., Mattsson, T. R., Nettelmann, N., & Redmer, R. 2009, *Phys. Rev. B*, 79, 054107
- Fukui, A., et al. 2011, *PASJ*, 63, 287
- Gibson, N. P., Pont, F., & Aigrain, S. 2011, *MNRAS*, 411, 2199
- Gibson, N. P., et al. 2012, *MNRAS*, 422, 753
- Gillon, M., et al. 2007, *A&A*, 472, L13
- Greiner, J., et al. 2008, *PASP*, 120, 405
- Henry, T. J., & McCarthy, Jr., D. W. 1993, *AJ*, 106, 773
- Howe, A. R., & Burrows, A. S. 2012, *ApJ*, 756, 176



- Ikoma, M., & Hori, Y. 2012, *ApJ*, 753, 66
- Kervella, P., Thévenin, F., Di Folco, E., & Ségransan, D. 2004, *A&A*, 426, 297
- Knutson, H. A., et al. 2011, *ApJ*, 735, 27
- Kotani, T., et al. 2005, *Nuovo Cimento C Geophysics Space Physics C*, 28, 755
- Lecavelier Des Etangs, A., Pont, F., Vidal-Madjar, A., & Sing, D. 2008a, *A&A*, 481, L83
- Lecavelier Des Etangs, A., Vidal-Madjar, A., Désert, J.-M., & Sing, D. 2008b, *A&A*, 485, 865
- Lecavelier Des Etangs, A., et al. 2010, *A&A*, 514, A72
- Lyon, S. P., & Johnson, J. D. 1992, Los Alamos Report No. LA-UR-92-3407.
- Mancini, L., et al. 2013, *ArXiv e-prints*
- Mandel, K., & Agol, E. 2002, *ApJ*, 580, L171
- Narita, N., Nagayama, T., Suenaga, T., Fukui, A., Ikoma, M., Nakajima, Y., Nishiyama, S., & Tamura, M. 2012, *ArXiv e-prints*
- Ohta, Y., Taruya, A., & Suto, Y. 2009, *ApJ*, 690, 1
- Pont, F., Knutson, H., Gilliland, R. L., Moutou, C., & Charbonneau, D. 2008, *MNRAS*, 385, 109
- Press, W. H., Teukolsky, S. A., Vetterling, W. T., & Flannery, B. P. 1992, *Numerical recipes in C. The art of scientific computing*, ed. Press, W. H., Teukolsky, S. A., Vetterling, W. T., & Flannery, B. P.
- Redfield, S., Endl, M., Cochran, W. D., & Koesterke, L. 2008, *ApJ*, 673, L87
- Saumon, D., Chabrier, G., & van Horn, H. M. 1995, *ApJS*, 99, 713
- Schwarz, G. 1978, *Ann. Statistics*, 6, 461
- Seager, S., & Sasselov, D. D. 2000, *ApJ*, 537, 916
- Sing, D. K., Désert, J.-M., Lecavelier Des Etangs, A., Ballester, G. E., Vidal-Madjar, A., Parmentier, V., Hebrard, G., & Henry, G. W. 2009, *A&A*, 505, 891
- Snellen, I. A. G., Albrecht, S., de Mooij, E. J. W., & Le Poole, R. S. 2008, *A&A*, 487, 357
- Snellen, I. A. G., de Kok, R. J., de Mooij, E. J. W., & Albrecht, S. 2010, *Nature*, 465, 1049
- Stevenson, K. B., et al. 2010, *Nature*, 464, 1161
- Valencia, D., Sasselov, D. D., & O’Connell, R. J. 2007, *ApJ*, 656, 545

- Vidal-Madjar, A., Lecavelier des Etangs, A., Désert, J.-M., Ballester, G. E., Ferlet, R., Hébrard, G., & Mayor, M. 2003, *Nature*, 422, 143
- Vidal-Madjar, A., et al. 2004, *ApJ*, 604, L69
- Yanagisawa, K., Kuroda, D., Yoshida, M., Shimizu, Y., Nagayama, S., Toda, H., Ohta, K., & Kawai, N. 2010, in *American Institute of Physics Conference Series*, Vol. 1279, American Institute of Physics Conference Series, ed. N. Kawai & S. Nagataki, 466–468
- Yanagisawa, K., et al. 2006, in *Society of Photo-Optical Instrumentation Engineers (SPIE) Conference Series*, Vol. 6269, Society of Photo-Optical Instrumentation Engineers (SPIE) Conference Series
- Yanagisawa, K., et al. 2008, in *Society of Photo-Optical Instrumentation Engineers (SPIE) Conference Series*, Vol. 7014, Society of Photo-Optical Instrumentation Engineers (SPIE) Conference Series

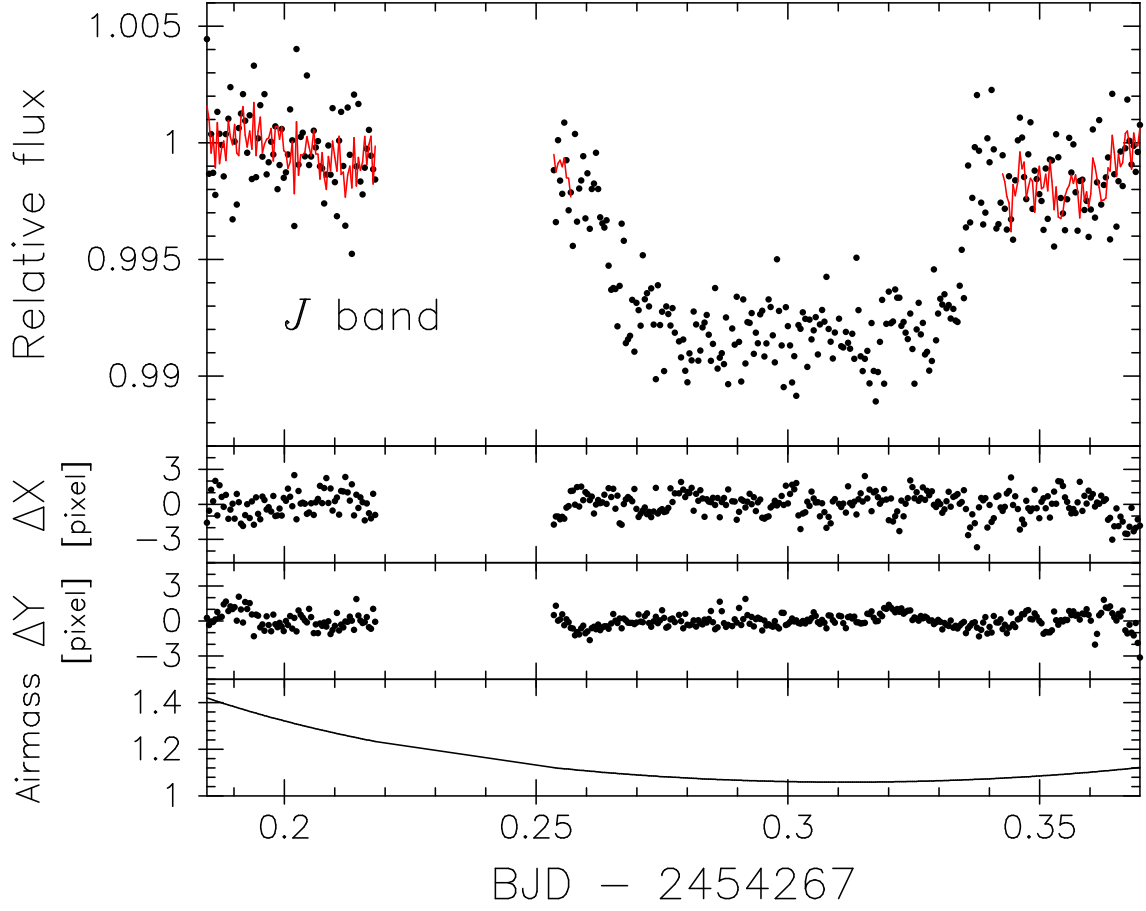


Fig. 1.— (Upper panel) The *J*-band uncorrected light curve of GJ3470b. The best-fit baseline model, which is as a function of airmass and stellar centroid displacements in X and Y directions, is over plotted as solid line in the OOT part. (Second panel) The stellar centroid displacements in X direction. (Third panel) The same as the second panel but in Y direction. (Bottom panel) The airmass variations.

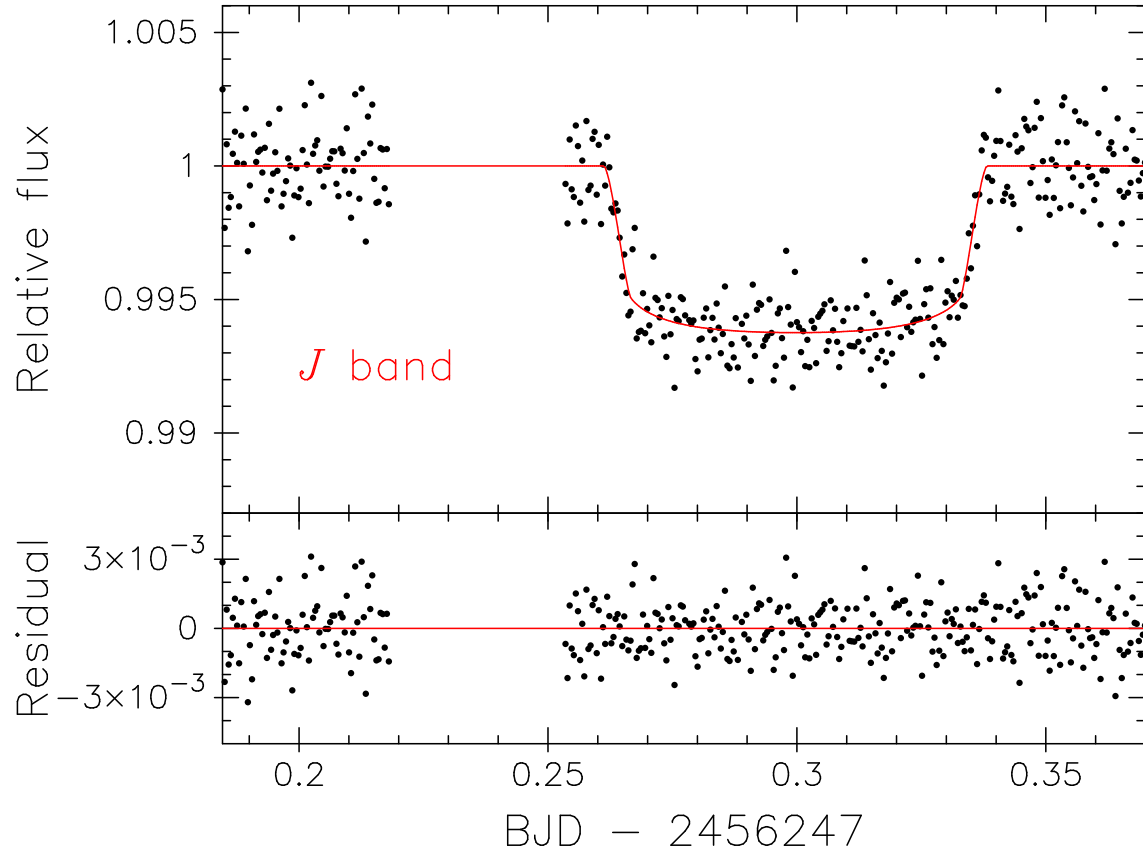


Fig. 2.— (Upper panel) The baseline-corrected *J*-band light curve. The best-fit transit model derived in Section 3.1 is shown as solid line. (Bottom panel) The residual light curve. The RMS of the residuals is  $1.18 \times 10^{-3}$ .

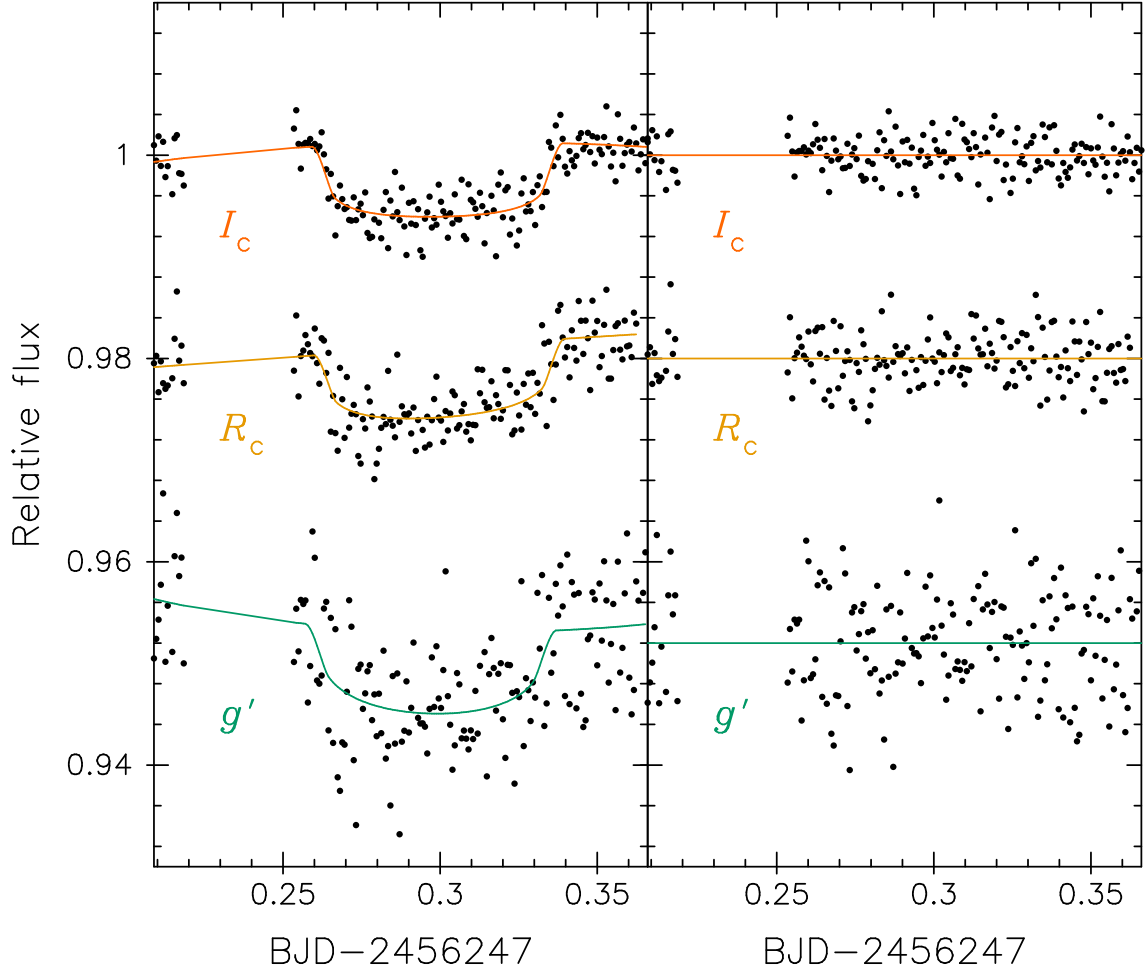


Fig. 3.— (Left panel) The uncorrected light curves of MITSuME  $I_c$ ,  $R_c$ , and  $g'$  bands, from top to bottom. The best-fit baseline models are over plotted as solid lines. For display, -0.02 and -0.048 are added in the  $R_c$  and  $g'$  light curves, respectively. (Right panel) The same as the left panel but residual light curves. The RMS of these residuals are  $1.78 \times 10^{-3}$ ,  $2.45 \times 10^{-3}$ , and  $5.27 \times 10^{-3}$ , for  $I_c$ ,  $R_c$ , and  $g'$  bands, respectively.

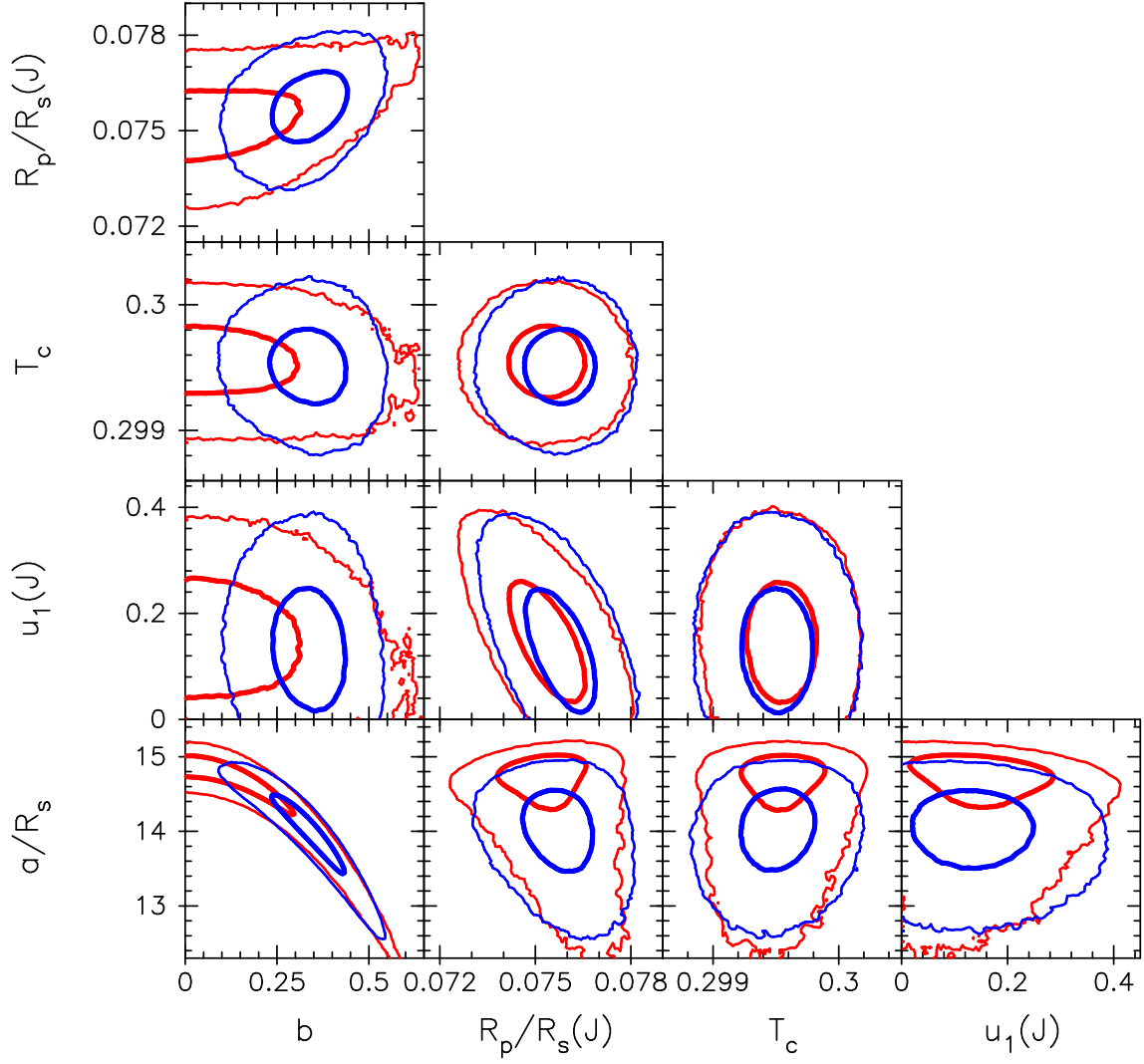


Fig. 4.— The two-dimensional 68.3% (thick lines) and 99.7% (thin lines) confidence regions for selected parameters calculated from the posterior probability distributions as a consequence of the MCMC analysis. The gray (red in online version) contours show the results from the MCMC analysis without any prior, while the black (blue in online version) contours indicate those with a  $b$  prior.

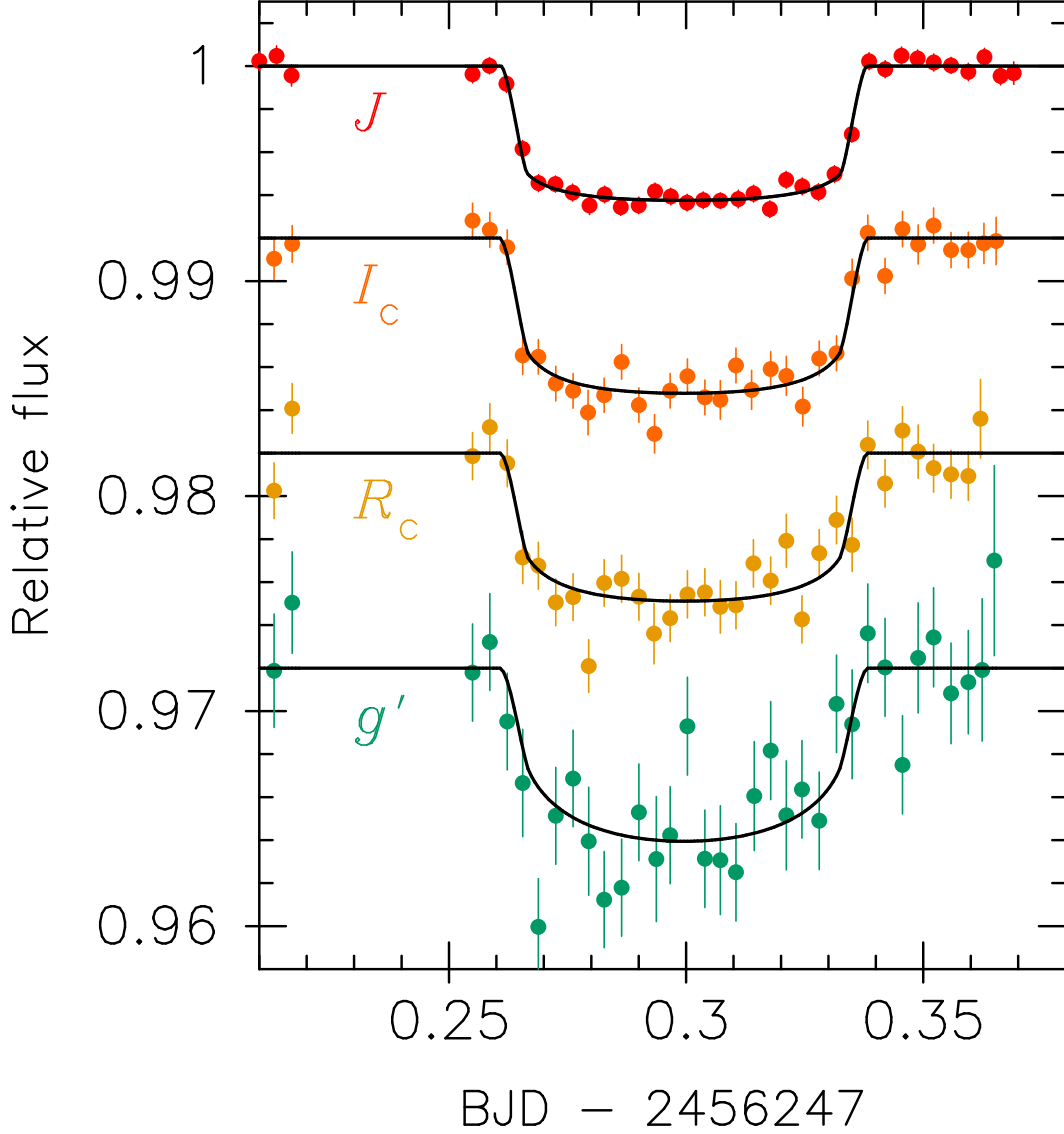


Fig. 5.— The overall light curves after the baseline correction, the error normalization, and 5-min binning. The  $J$ -,  $I_c$ -,  $R_c$ -, and  $g'$ -band light curves are shown from top to bottom. The offsets of -0.08, -0.18, and -0.28 are added for the  $I_c$ -,  $R_c$ -, and  $g'$ -band light curves, respectively, for clarify. The best-estimated transit models derived from the MCMC analysis without  $b$  prior are shown as solid lines.

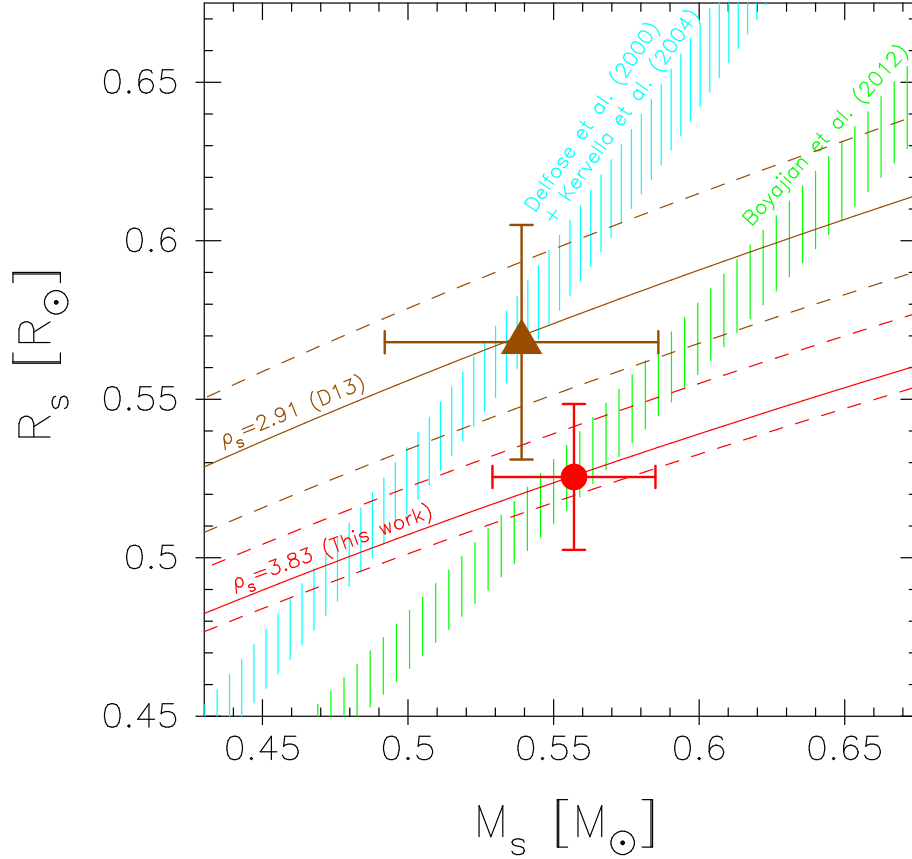


Fig. 6.— Comparison of  $M_s$  and  $R_s$  calibrations between this work and D13. The stellar density derived in this work (MCMC analysis without  $b$  prior) and that by D13 are indicated by lower (red in online) and upper (brown in online) lines. Solid and dashed lines represent median and  $1\sigma$  uncertainties, respectively. The mass-radius relation we adopted (Equation (4) in Boyajian et al. (2012)) is shown as right (green in online) shaded region ( $1\sigma$  region), while the mass-radius relation for GJ3470 drawn by connecting a mass-luminosity (Delfosse et al. 2000) and a diameter-color-luminosity (Kervella et al. 2004) relations are shown as left (light-blue in online) shaded region, where 2% uncertainty in  $R_s$  is adopted. The  $M_s$  and  $R_s$  values derived in this work and by D13 are indicated as circle and triangle, respectively.



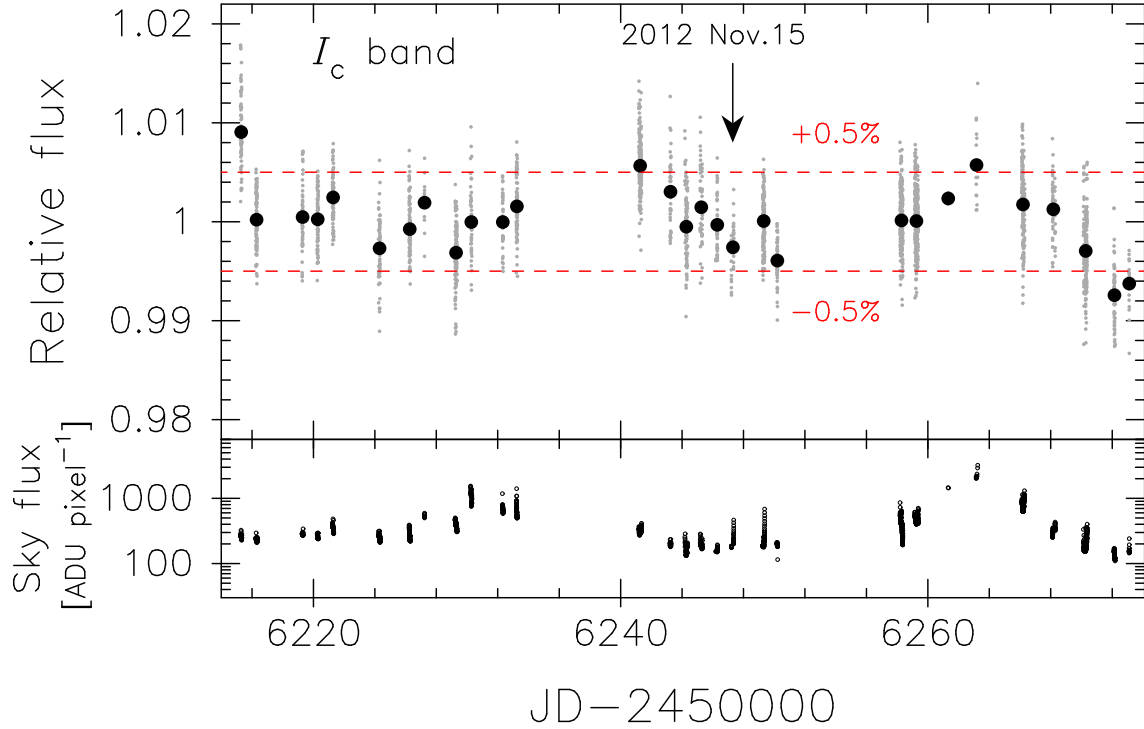


Fig. 7.— (Upper panel) A long-term  $I_c$ -band light curve for GJ3470 obtained by the 50-cm MIT-SuME telescope. Transit part is eliminated in this light curve. Individual 60-sec exposure data and nightly-averaged data are indicated as gray and black points, respectively. RMS of the black points is 0.33%, while peak-to-valley variations is  $\sim 1\%$ . The  $\pm 0.5\%$  variation level is shown as dashed line. The transit-observed date is indicated by an arrow. (Bottom panel) Sky-flux variations. A possible correlation between the light curve and sky flux can be seen after JD-2450000  $\sim$  6258.

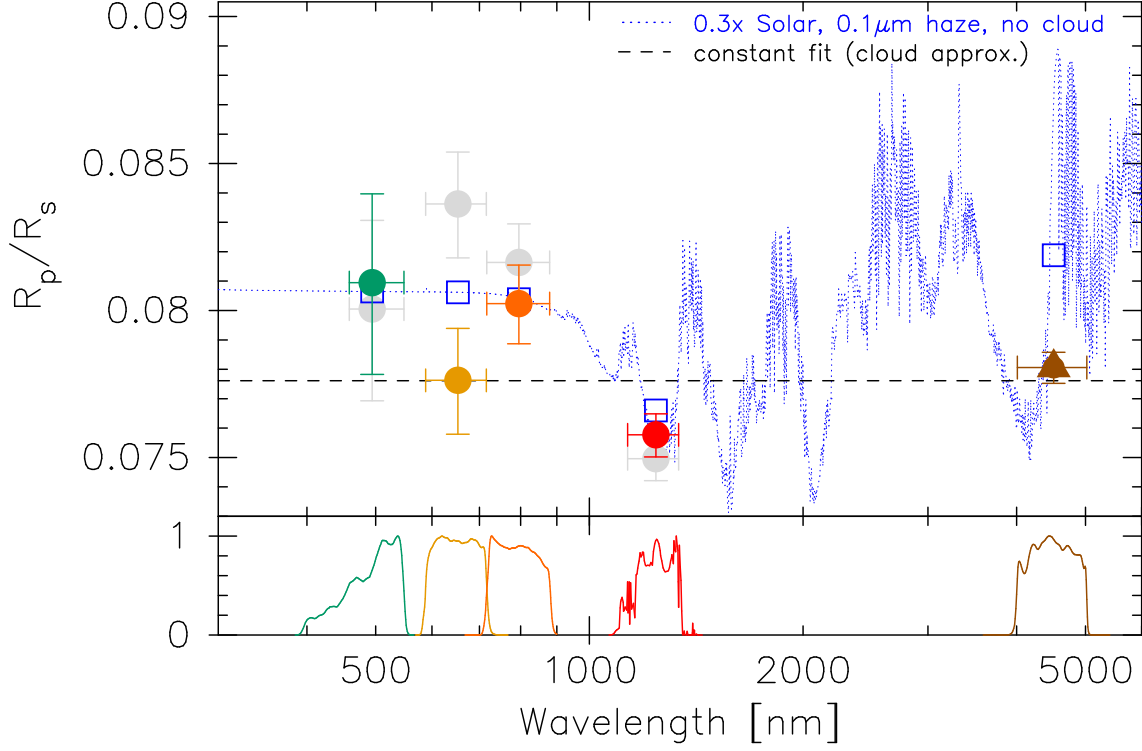


Fig. 8.— (Top panel) Wavelength dependence of the observed  $R_p/R_s$  values for GJ3470b. The data derived from the MCMC analysis with  $b$  prior are indicated as filled circles, with green, yellow, orange, and red for the  $g'$ ,  $R_c$ ,  $I_c$ , and  $J$  bands, respectively. The *Spitzer*/IRAC 4.5- $\mu m$  data obtained by D13 is shown as brown triangle. The horizontal values and error bars denote the weighted center and the width at half maximum of the respective transmission curves shown in the bottom panel, respectively. The horizontal dashed line indicates the weighted mean of the five  $R_p/R_s$  values ( $=0.07761$ ), representing an approximated fully-clouded atmospheric spectrum. The blue dotted line indicates a model spectrum for a  $0.3 \times$  Solar-abundance cloud-free atmosphere with  $T = 700$  K and containing 0.1- $\mu m$  sized tholin particles with a density of  $1000 \text{ cm}^{-3}$ , being drawn by scaling a model spectrum provided by Howe & Burrows (2012) so as to fit the scale height of GJ3470b. The blue squares indicate the integrated cloud-free model spectrum over the respective passbands. The gray circles indicate the impact of possible systematics due to the baseline-model selection; the original value is shifted by the difference of  $R_p/R_s$  that would be produced if an alternative baseline model was adopted. (Bottom panel) The transmission curves for the respective bands.

Table 1. Observing Log

Observing Date	Filter	Telescope	Exp. time [s]	$N_{\text{all}}$ <sup>a</sup>	Airmass variation
2012 November 15	$J$	OA0 188 cm	30	352	1.42 $\rightarrow$ 1.06 $\rightarrow$ 1.12
2012 November 15	$I_c$	MITSuME 50 cm	60	165	1.28 $\rightarrow$ 1.06 $\rightarrow$ 1.11
2012 November 15	$R_c$	MITSuME 50 cm	60	162	1.28 $\rightarrow$ 1.06 $\rightarrow$ 1.11
2012 November 15	$g'$	MITSuME 50 cm	60	164	1.28 $\rightarrow$ 1.06 $\rightarrow$ 1.11

<sup>a</sup> The total number of observed data used for analyses, i.e., after omitting outliers.

Table 2. Fitting results for  $J$ -band data for different baseline models <sup>a</sup>

Variables { $\mathbf{X}$ }	BIC <sub>oot</sub>	RMS <sub>oot</sub> ( $\times 10^{-3}$ )	$\chi^2_{\text{all}}$ <sup>b</sup>	$R_p/R_s$ <sup>c</sup> ( $\times 10^{-2}$ )	$a/R_s$ <sup>c</sup>	$b$ <sup>c d</sup>	$T_c$ <sup>c</sup> [BJD <sub>TDB</sub> -2456247]
$z$	224.2	1.61	449.3	$7.754 \pm 0.098$	$14.91^{+1.2}_{-0.33}$	$0.00 \pm 0.21$	$0.29949 \pm 0.00025$
$z, dx, dy$	<b>171.4</b>	<b>1.35</b>	<b>299.5</b>	<b><math>7.513 \pm 0.082</math></b>	<b><math>14.86^{+0.11}_{-0.44}</math></b>	<b><math>0.00 \pm 0.24</math></b>	<b><math>0.29971 \pm 0.00022</math></b>
$z, t, dx, dy$	176.3	1.35	299.5	$7.483 \pm 0.082$	$14.87^{+0.12}_{-0.44}$	$0.00 \pm 0.24$	$0.29974 \pm 0.00022$
$t, t^2, dx, dy$	176.4	1.35	299.9	$7.432 \pm 0.083$	$14.88^{+0.11}_{-0.44}$	$0.00 \pm 0.24$	$0.29973 \pm 0.00022$

<sup>a</sup> The fitting results for the adopted baseline model are indicated as bold text.

<sup>b</sup> The subscript ‘all’ denotes that the entire light curve is used for the  $\chi^2$  calculation.

<sup>c</sup> The uncertainties are calculated after the flux errors are rescaled so that the reduced  $\chi^2_{\text{all}}$  value is unity.

<sup>d</sup> The  $b$  value is allowed to be minus in the fitting process, but the absolute value is used for modeling a transit light curve.

Table 3. Fitting results for the MITSuME data for different baseline models <sup>a</sup>

Variables $\{\mathbf{X}\}$	BIC	RMS ( $\times 10^{-3}$ )	$R_p/R_s$ ( $\times 10^{-2}$ )
MITSuME $I_c$			
<b><math>\mathbf{z}</math></b>	<b>185.5</b>	<b>1.81</b>	<b><math>7.97 \pm 0.13</math></b>
$z, t$	192.1	1.82	$8.06 \pm 0.12$
$t, t^2$	191.8	1.82	$8.11 \pm 0.12$
MITSuME $R_c$			
$z$	186.5	2.50	$8.32 \pm 0.17$
<b><math>\mathbf{z}, \mathbf{t}</math></b>	<b>186.5</b>	<b>2.46</b>	<b><math>7.72 \pm 0.17</math></b>
$t, t^2$	186.5	2.46	$7.74 \pm 0.17$
MITSuME $g'$			
<b><math>\mathbf{z}</math></b>	<b>184.5</b>	<b>5.12</b>	<b><math>8.16 \pm 0.30</math></b>
$z, t$	189.6	5.12	$8.08 \pm 0.30$
$t, t^2$	189.7	5.12	$8.07 \pm 0.30$

<sup>a</sup> The fitting results for the adopted baseline models are indicated as bold text.

Table 4. MCMC results for transit parameters

Parameter	D13	This work (w/o $b$ prior)	This work (w/ $b$ prior)
Impact parameter, $b$ ( $\equiv a \cos i / R_s$ )	$0.40^{+0.06}_{-0.08}$	$< 0.281$ (1- $\sigma$ upper limit)	$0.337^{+0.067}_{-0.070}$
Scaled semi-major axis, $a/R_s$	$13.42^{+0.55}_{-0.53}$	$14.70^{+0.17}_{-0.43}$	$14.02^{+0.33}_{-0.39}$
Mid transit time, $T_c$ [BJD <sub>TDB</sub> - 2450000]	$6090.47690 \pm 0.00015$	$6247.29954 \pm 0.00019$	$6247.29951 \pm 0.00020$
Planet-to-star radius ratio			
$R_p/R_s$ (4.5 $\mu$ m)	$0.07806^{+0.00052}_{-0.00054}$	...	...
$R_p/R_s$ ( $J$ )	...	$0.07536 \pm 0.00079$	$0.07577^{+0.00072}_{-0.00075}$
$R_p/R_s$ ( $I_c$ )	...	$0.0797 \pm 0.0014$	$0.0802 \pm 0.0013$
$R_p/R_s$ ( $R_c$ )	...	$0.0770 \pm 0.0019$	$0.0776 \pm 0.0018$
$R_p/R_s$ ( $g'$ )	...	$0.0800 \pm 0.0030$	$0.0809 \pm 0.0031$
Limb-darkening coefficients			
$u_1$ ( $J$ )	...	$0.149 \pm 0.074$	$0.137^{+0.077}_{-0.073}$
$u_2$ ( $J$ )	...	$0.255$ (fixed)	$0.255$ (fixed)
$u_1$ ( $I_c$ )	...	$0.20 \pm 0.11$	$0.19 \pm 0.11$
$u_2$ ( $I_c$ )	...	$0.338$ (fixed)	$0.338$ (fixed)
$u_1$ ( $R_c$ )	...	$0.26 \pm 0.15$	$0.25 \pm 0.15$
$u_2$ ( $R_c$ )	...	$0.322$ (fixed)	$0.322$ (fixed)
$u_1$ ( $g'$ )	...	$0.486$ (fixed)	$0.486$ (fixed)
$u_2$ ( $g'$ )	...	$0.289$ (fixed)	$0.289$ (fixed)

Table 5. Physical parameters

Parameter	D13	This work (w/o $b$ prior)	This work (w/ $b$ prior)
<i>Stellar parameters</i>			
Stellar mass, $M_s$ [ $M_\odot$ ]	$0.539^{+0.047}_{-0.043}$	$0.557^{+0.028}_{-0.020}$	$0.594^{+0.029}_{-0.026}$
Stellar radius, $R_s$ [ $R_\odot$ ]	$0.568^{+0.037}_{-0.031}$	$0.526^{+0.023}_{-0.011}$	$0.563^{+0.024}_{-0.020}$
Stellar density, $\rho_s$ [ $\rho_\odot$ ]	$2.91^{+0.37}_{-0.33}$	$3.83^{+0.14}_{-0.32}$	$3.32^{+0.24}_{-0.27}$
Stellar surface gravity, $\log g_s$ [cgs]	$4.658 \pm 0.030$	$4.741^{+0.009}_{-0.019}$	$4.710^{+0.016}_{-0.019}$
<i>Planetary parameters</i>			
Orbital period, $P$ [days]	$3.33671 \pm 0.00005$	$3.336652 \pm 0.000005$	$3.336651 \pm 0.000005$
Semi-major axis, $a$ [AU]	$0.03557^{+0.00096}_{-0.00100}$	$0.03596^{+0.00059}_{-0.00044}$	$0.03674^{+0.00059}_{-0.00054}$
Planetary mass, $M_p$ [ $M_\oplus$ ]	$13.9^{+1.5}_{-1.4}$	$14.1 \pm 1.3$	$14.6 \pm 1.4$
Planetary radius, $R_p$ [ $R_\oplus$ ]	$4.83^{+0.22}_{-0.21}$	$4.32^{+0.21}_{-0.10}$	$4.65^{+0.22}_{-0.18}$
Planetary density, $\rho_p$ [g cm <sup>-3</sup> ]	$0.72^{+0.13}_{-0.12}$	$0.94 \pm 0.12$	$0.80 \pm 0.11$
Planetary surface gravity, $g_p$ [m s <sup>-2</sup> ]	$5.75^{+0.85}_{-0.86}$	$7.25^{+0.75}_{-0.78}$	$6.58^{+0.72}_{-0.70}$